PLOS ONE

RESEARCH ARTICLE

Classification of neurons in the adult mouse cochlear nucleus: Linear discriminant analysis

Paul B. Manis[1]*, **Michael R. Kasten**[1], **Ruili Xie**[2]

1 Department of Otolaryngology/Head and Neck Surgery, The University of North Carolina at Chapel Hill, Chapel Hill, North Carolina, United States of America, **2** Department of Otolaryngology, The Ohio State University, Columbus, Ohio, United States of America

* paul_manis@med.unc.edu

Citation: Manis PB, Kasten MR, Xie R (2019) Classification of neurons in the adult mouse cochlear nucleus: Linear discriminant analysis. PLoS ONE 14(10): e0223137. https://doi.org/10.1371/journal.pone.0223137

Editor: Manuel S. Malmierca, Universidad de Salamanca, SPAIN

Received: July 16, 2019

Accepted: September 13, 2019

Published: October 3, 2019

Data Availability Statement: Data is available on Figshare at the following DOI: 10.6084/m9.figshare.8854352.v1. The repository includes raw data traces in NWB format, two databases of analysis results, and code to reproduce the figures.

Funding: PBM and MRK were supported by R01 DC004551, from the National Institute on Deafness and other Communicative Disorders of the National Institutes of Health. The funders had no role in study design, data collection and analysis, decision to publish, or preparation of the manuscript. RX was supported by R03 DC013396, from the

Abstract

The cochlear nucleus (CN) transforms the spike trains of spiral ganglion cells into a set of sensory representations that are essential for auditory discriminations and perception. These transformations require the coordinated activity of different classes of neurons that are embryologically derived from distinct sets of precursors. Decades of investigation have shown that the neurons of the CN are differentiated by their morphology, neurotransmitter receptors, ion channel expression and intrinsic excitability. In the present study we have used linear discriminant analysis (LDA) to perform an unbiased analysis of measures of the responses of CN neurons to current injections to objectively categorize cells on the basis of both morphology and physiology. Recordings were made from cells in brain slices from CBA/CaJ mice and a transgenic mouse line, NF107, crossed against the Ai32 line. For each cell, responses to current injections were analyzed for spike rate, spike shape, input resistance, resting membrane potential, membrane time constant, hyperpolarization-activated sag and time constant. Cells were filled with dye for morphological classification, and visually classified according to published accounts. The different morphological classes of cells were separated with the LDA. Ventral cochlear nucleus (VCN) bushy cells, planar multipolar (T-stellate) cells, and radiate multipolar (D-stellate) cells were in separate clusters and separate from all of the neurons from the dorsal cochlear nucleus (DCN). Within the DCN, the pyramidal cells and tuberculoventral cells were largely separated from a distinct cluster of cartwheel cells. principal axes, whereas VCN cells were in 3 clouds approximately orthogonal to this plane. VCN neurons from the two mouse strains overlapped but were slightly separated, indicating either a strain dependence or differences in slice preparation methods. We conclude that cochlear nucleus neurons can be objectively distinguished based on their intrinsic electrical properties, but such distinctions are still best aided by morphological identification.

Introduction

Neurons of the mammalian cochlear nucleus exhibit a variety of responses to intracellular current injection, reflecting the distinct expression of collections of ion channels amongst

National Institute on Deafness and other Communicative Disorders of the National Institutes of Health. The funders had no role in study design, data collection and analysis, decision to publish, or preparation of the manuscript.

Competing interests: The authors have declared that no competing interests exist.

different classes. However, even within a class, such as bushy cells, individual cells may express specific conductances at different magnitudes [1–3], leading to diversity in excitability features such as action potential threshold, action potential height, and rheobase. In spite of this variability, cells of a given morphological class appear to possess common properties that have been used to identify cells on the basis of their electrical signatures alone [4–12].

Quantitative methods for identifying cell classes have been explored in the context of the myriad interneuronal populations in cortex [13], within the olfactory bulb [14] and across neuronal populations throughout the brain [15]. These methods rely on systematic measurement of distinct features of intrinsic excitability such as action potential shape, firing rates, passive membrane measures, and responses to hyperpolarization, and have used principal components analysis (PCA), support vector machine model, or stepwise linear regressions. Within the cochlear nucleus, application of an hierarchical clustering analysis to *in vivo* single unit data provided evidence for partial separation of unit response types in the gerbil AVCN [16], although further analysis (using PCA) suggested that there was extensive overlap between cell classes.

Here we apply linear discriminant analysis [17] to the problem of separating cell classes in the cochlear nucleus based on intrinsic excitability. Whereas PCA separates classes by finding the axes that maximize the variance within a data set, and does not rely on labels, LDA maximizes the separation between classes, utilizing label (e.g., class) information. We find that LDA is an effective tool for segregating morphologically defined cell classes based on their intrinsic excitability. However, the results indicate the presence of some overlap between the properties of certain classes, or that features other than dendritic morphology are needed to provide more exclusive cell classification. Such a classification tool should be useful in future studies of the excitability of cochlear nucleus neurons following hearing loss, as a way of objectively assessing how the excitability of neurons changes.

Materials and methods

Brain slice preparation

Whole cell tight-seal recordings were made in brain slices from adult CBA/CaJ (P28-69) and NF107::Ai32 (P31-166) mice. The NF107::Ai32 mice are the F1 cross of the NF107 mouse line, originally from the GENSAT Consosrtium [18], and the channel rhodopsin (ChR2) expressing line Ai32 [19], and so are on a mixed CD-1, C57Bl/6J and FVB background. The data from the CBA/CaJ mice were taken from a previous series of studies [11,20]. Data from the NF107 mice were included because we had a substantial dataset of cells recorded under consistent conditions (electrode and extracellular solutions), along with overlap of cell types with the dataset from CBA/CaJ mice. The ChR2 was not activated during these experiments. Data from the NF107::Ai32 mice were taken from unpublished work (Kasten, Ropp and Manis). CBA/CaJ mice were of either sex (bushy cells: F:2, M:9, undetermined: 7; planar multipolar cells: F:10, M:14, undetermined: 7; radiate multipolar cells: F:4, M:20, undetermined: 8), whereas the NF107::AI32 mice were only males, as the Cre driver is carried on the Y chromosome. CBA/CaJ mice were prepared following anesthesia (100 mg/kg ketamine and 10 mg/kg xylazine), and decapitation, with slicing in warm ACSF. The NF107::Ai32 slices were prepared using the same anesthesia followed by transcardial perfusion with an NMDG-based solution [21].

The recording ACSF contained (in mM): 122 NaCl, 3 KCl, 1.25 NaH_2PO_4, 25 $NaHCO_3$, 20 glucose, 3 myo-inositol, 2 sodium pyruvate, 0.4 ascorbic acid, 2.5 $CaCl_2$, and 1.5 $MgSO_4$. Electrodes contained (in mM): 126 K-gluconate, 6 KCl, 2 NaCl, 10 HEPES, 0.2 EGTA, 4 Mg-ATP, 0.3 Tris-GTP, and 10 Tris-phosphocreatine, with pH adjusted to 7.2 with KOH. Recordings were made with a MultiClamp 700B (Molecular Devices, San Jose, CA) amplifier, low-pass filtered at 6kHz, and digitized at 10–20 kHz with 16-bit A-D converters (National Instruments,

Austin TX). Stimulus presentation and acquisition were controlled by either a custom Matlab® program (Mathworks, Boston MA, R2016) or by *acq4* [22]. All animal procedures were approved by the University of North Carolina Institutuional and Animal Care Committee (protocols 12–253, 15–253 and 18–160).

Measurements

For each cell, responses to current injections (100–500 msec duration, ranging from -1 to 4 nA) were analyzed. Data from either acquisition program were converted to a common format for analysis by Python (V3.6) scripts. Passive measures included input resistance (from the slope of the current-voltage relationship just below rest), resting membrane potential, membrane time constant (measured from responses to small hyperpolarizing current steps that produced 2–10 mV voltage deflections), the magnitude of the hyperpolarization sag [23] and the time constant for the sag measured when the steady-state voltage was near -80 mV. The magnitude of the sag was computed as a ratio for comparison across cells, as the steady-state hyperpolarization from rest (measured at the end of a 100 or 500 ms step) divided by the peak hyperpolarization from rest [23]. Active measures included action potential height (measured from rest to action potential peak), first spike half-width (measured at half the action potential height from rest), afterhyperpolarization depth (measured from rest to the first afterhyperpolarization peak), an adaptation index measured near firing threshold (see below), the maximal number of rebound spikes that occurred after the offset from hyperpolarizing steps, the coefficient of variation of interspike intervals, and the slope of the firing rate versus current curve for the first 3 current levels above threshold. Cells were filled with dyes (AlexaFluor 488 for CBA/CaJ mice; tetramethylrhodamine biocytin for the NF107:Ai32 mice) for morphological classification, and visually classified according to published accounts, based on digital images and image stacks collected at low (4X) and high (40-63X) power either during or immediately after each cell was recorded.

Planar and radiate multipolar cells were classified according to the orientiation of their principal dendrites (as in [11,24]); planar multipolar cells have dendrites that are parallel to the fascicles of auditory nerve fibers, whereas the radiate multipolar cells have dendrites that can extend across the auditory nerve fascicles as well as running parallel to the fascicles. Bushy cells were classified based on having one or two primary dendrites that branch less than ~100 μm from the cell body [5,25–29]. For neurons from the VCN of CBA/CaJ mice, the morphological classifaction was drawn from our previous work [11]. In DCN, pyramidal cells were identified as bipolar neurons whose long axis was approximately orthogonal to the surface of the nucleus, with apical dendrites that had a mixture of small and longer spines, and at least one basal dendrite [30,31]. Basal dendrites were devoid of spines except at their very distal ends where they had a spray of short branches. Cartwheel cells were identified by their location in the molecular layer, lack of basal dendrites, a dense array of small spines along the dendrites in the molecular layer, and often (but not always) an characteristic curvature of the denrdrites and obtuse branching angles [7,10,32–34]. Tuberculoventral cells were identified by their location in the deep layer, with thin branching dendrites ascending towards the pyramidal cell layer, and occasionally dendrites that branched within the deep layer or which went deeper [12,35,36]. Tuberculoventral cells had few spines.

Adaptation was measured for the lowest two levels of current that elicited spikes as:

$$\frac{-2}{N}\sum_{i=0}^{i=N}\left(\frac{t_i}{t_d}-0.5\right)$$

Where t_i is the time of the i^{th} spike in the trace, t_d is the trace duration, and N is the number of spikes. This measure ranges from -1 to 1. Neurons that fire regularly without adaptation throughout the trace will have an index of 0. Neurons that fire preferentially only at the onset of the trace will have an index of 1, whereas those that fire near the end of the trace will have an index of -1. Thus, bushy cells will have an index of 1, stellate cells and tuberculoventral cells will usually have an index near 0, and pyramidal cells may have a negative index, depending on the delay to the first spike. Note that this measure depends on the current level that is used relative to the spike threshold, as well as the current duration. The adaptation measured at the threshold current was found to be uninformative in preliminary analyses, and so the only adaptation computed from the next higher current that evoked spikes was used.

All absolute voltage measurements are corrected for a -11 mV junction potential for the K-gluconate electrodes. All other voltage measurements are differential (action potential height from peak to the minimum of the following AHP) and are independent of the junction potential.

Computed measures were then analyzed by LDA and PCA using standard libraries in Python (scikit-learn v0.20, Python 3.6), and in R (3.5, using the packages DisplayR and flipMultivariates). For each method, 5 components were computed (1 fewer than the number of classes). Accuracy of the classification was calculated using 10-fold cross-validation (k-fold splitting method), using the *cross_val_score* routine from sckit-learn. Each run splits the data into training and test sets, and uses the training set to generate a new classifier. The test data is then evaluated with the new classifier to determine the accuracy for each split. The accuracy is represented as the average and standard deviation over 10 different splits.

Results

The discharge patterns of cochlear nucleus neurons have been reported in a series of studies over the years from multiple laboratories using similar, but not identical recording conditions. Fig 1 shows the intrinsic physiology of example cells from six major morphological classes as recorded in our dataset. Briefly, bushy cells (Fig 1A) fire 1–3 action potentials at the onset of depolarizing current injections, and are silent thereafter [4,5]. At higher current levels, oscillatory membrane responses, which may represent axonally initiated action potentials, are sometimes visible. In response to hyperpolarizing pulses, bushy cells can show a slow sag in membrane potential, and following the hyperpolarizing step can generate an anodal break spike. The planar multipolar cells (Fig 1B) fire regularly in response to depolarizing current injections, and also show a slow sag in response to hyperpolarizing current steps; they can also show anodal break spikes [11,23]. Radiate multipolar cells also fire regularly in response to depolarization, sometimes exhibiting an adapting spike train. They show a rapid sag in response to hyperpolarization, and frequently have anodal break spikes. As noted previously [11], radiate multipolar cells also may fire only at the onset of a weak depolarizing current pulse. Pyramidal (fusiform) cells of the dorsal cochlear nucleus fire regularly [9,36,37], and may have a long delay to the first spike or a long first interspike interval [36,38,39]. In the adult mice studies here, these cells do not show a prominent sag, but do show a rapidly activating rectification in response to hyperpolarizing steps, which is likely generated by K_{ir} channels [40]. Cartwheel cells show mixed single-spiking regular firing and burst firing [7,10]. The tuberculoventral neurons show regular firing, and often have trains of rebound spikes after hyperpolarization [12,35]. The principal cell database included 18 bushy cells, 31 planar multipolar cells, 32 radiate multipolar cells, 38 pyramidal cells, 12 cartwheel cells, and 31 tuberculoventral cells. Additional cell classes (all from the DCN) had too few cells for effective classification. These included 1 "Type-B" cell [31], 1 chestnut cell [41], 7 giant cells, 2 "horizontal bipolar" cells (small neurons in the pyramidal cell layer of the DCN with a bipolar morphology where the moderately spiny dendrites reside mainly within the

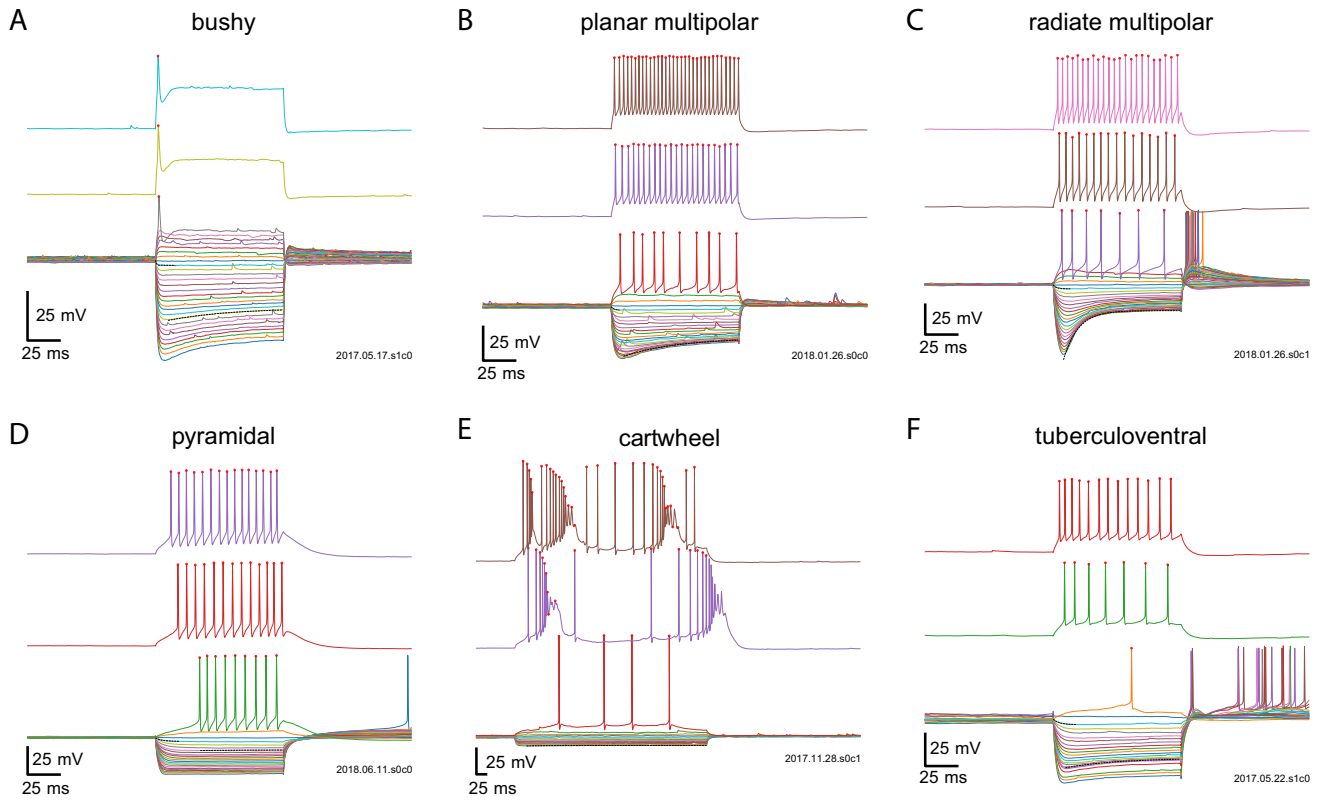

Fig 1. Examples of discharge patterns and passive responses, for different levels of current injection for 6 classes of cochlear nucleus neurons. A. Bushy; B. planar multipolar; C. radiate multipolar; D. pyramidal; E. cartwheel; F. tuberculoventral. Red dots indicate spikes evoked by current injection.

https://doi.org/10.1371/journal.pone.0223137.g001

pyramidal cell layer), 2 molecular layer stellate cells [42], 3 unipolar brush cells [41,43], and 3 cells that could not clearly be identified on comparison with the literature. These were not included in the analyses.

In order to classify the principal cell types, we extracted a set of measurements from the subthreshold current-voltage relationships and from suprathreshold spikes (N = 162 cells). These are illustrated in Figs 2 and 3. Fig 2 summarize the passive properties of the cells (columns) against the cell types (rows). From this, differences in the resting membrane potential, input resistances and time constants can be appreciated between the groups. In addition, measurements of the time constant of the hyperpolarizing sag, and a previously-used measure [23], the B/A sag ratio, also show clear differences between the cells, with neurons from the DCN generally showing weaker I_h.

Fig 3 shows measures of action potential shape and firing properties. Again, population-based distinctions are evident, such as the relatively small and wide action potentials of bushy cells, and the tendency of tuberculoventral and some cartwheel cells to show rebound responses, and the wide coefficient of variation of firing of the cartwheel cells. The firing rate slope measured near threshold also was lowest for bushy, pyramidal and cartwheel cells, and highest for the planar and radiate multipolar cells, and tuberculoventral cells.

Next, we submitted the data to a LDA, using all of the parameters measured in Figs 2 and 3. Data were first standardized for each measure before being submitted to the LDA. The standardization rescaled the individual measurements for each measurement type so that it had a zero mean and a unit standard deviation. The LDA was run with 5 components, and these accounted for 55.4, 21.6, 14.0, 8.0, and 1.0% of the overall variance. Fig 4 illustrates the first 3

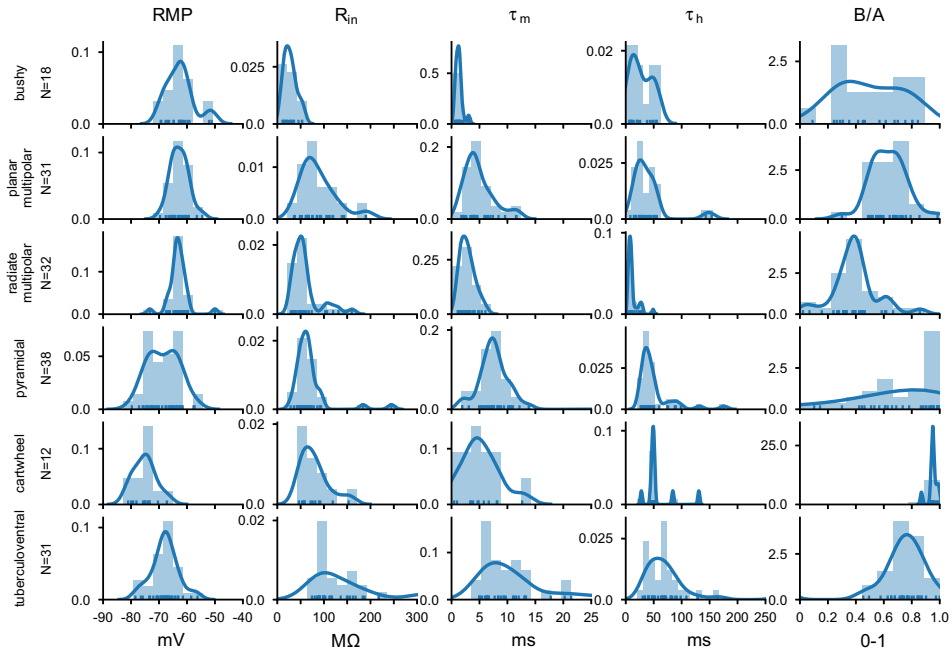

Fig 2. Summary of passive measurements from responses to hyperpolarizing current pulses across the population of CN neurons. RMP: resting membrane potential; R_{in}: input resistance; τ_m: membrane time constant; τ_h: time constant of repolarizing sag from traces near -80 mV; B/A: steady-state over peak voltage deflection for hyperpolarizing sag (see Materials and Methods and [23]). The ordinate indicates the population density based on the kernel density estimate (blue line). The histograms shows the distribution of values from the population cells for each type and measure.

https://doi.org/10.1371/journal.pone.0223137.g002

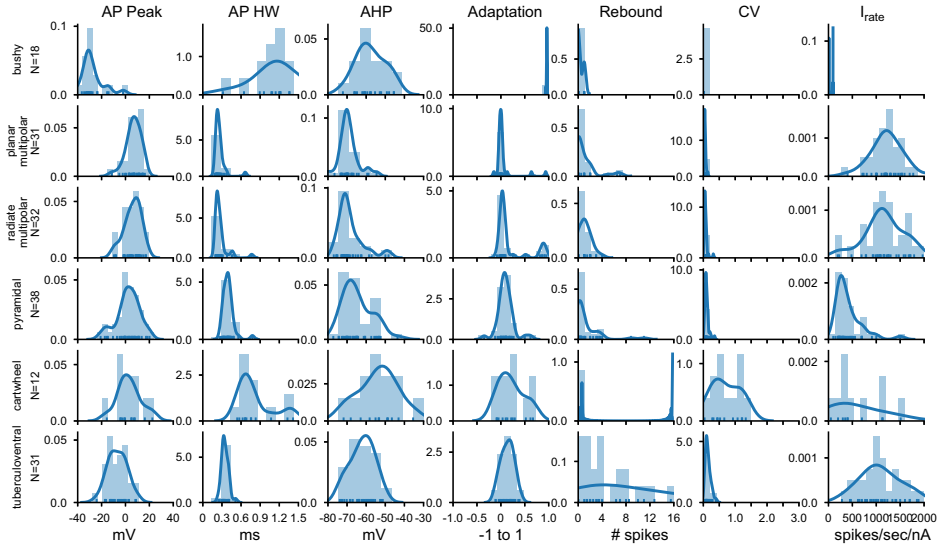

Fig 3. Summary of action potential shape and firing patterns across the population of CN neurons. AP Peak: action potential peak potential; APHW: action potential half-width; AHP: action potential afterhyperpolarization; Adaptation: adaptation calculated from the response to a suprathreshold current injection; Rebound: count of rebound action potential after the end of the hyperpolarizing current injection; CV: coefficient of variation of interspike intervals; I_{rate}: slope of the current-firing relationship for current levels just above spike threshold. The ordinate indicates the population density based on the kernel density estimate (blue line). The histograms show the distribution of values from the population cells for each type and measure.

https://doi.org/10.1371/journal.pone.0223137.g003

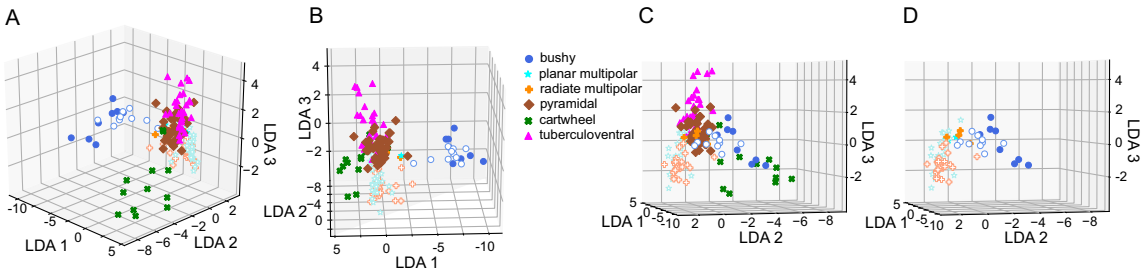

Fig 4. LDA with supervised clustering by cell morphology. A. The first 3 (largest) LDA components are shown in a perspective view. The axes represent the projections of each cell on to the 3 largest components from the standardized data (zero mean, unit standard deviation; therefore there are no units). Note the clear separation of the bushy cell and cartwheel cells populations from the rest of the CN neurons. Although the other populations are close together, they are also separated as can be appreciated by comparing the different views. Cells from CBA/CaJ mice are shown with open symbols; cells from the NF107 mice are shown with closed symbols. B, C. Two other perspective views (rotated) of the same data as in A. D. A view of the data for the VCN cells only (bushy, planar multipolar and radiate multipolar) for clarity. This is the same perspective view as panel C.

https://doi.org/10.1371/journal.pone.0223137.g004

components of the LDA, with each cell colored by its classified type, in 3 views (Fig 4A, 4B and 4C). The LDA effectively separated the different types of cells into distinct spaces. The bushy and cartwheel cells were the most separated from the remainder of the regular firing cells. Interestingly these two cell groups did not form tight clusters, suggesting some diversity in their properties. The pyramidal and tuberculoventral cells were clustered next to each other, although with minimal overlap. The radiate and planar multipolar cells formed two slightly overlapping clusters that were largely separate from all other cell classes. Note that although most of the bushy, planar and radiate multipolar cells were recorded in CBA/CaJ mice, those cells recorded from the NF107::Ai32 mice (FVB and C57Bl/6 backgrounds; solid symbols) were close to the measures of the CBA/CaJ populations, although they were slightly separated in one of the first 3 axes, as more clearly seen in Fig 4D, where only cells from the VCN are shown. A 10-fold cross-validation of the LDA yielded an estimated accuracy of 0.79 (± 0.31).

We also submitted the data set to a standard principal components analysis, following the same standardization across cells for each measure (Fig 5). In this case, the supervisory classifier (cell morphology) was not used in the initial classification. The PCA resulted in clusters of cells from the same morphological class, but these had greater overlap than with the LDA. A 10-fold cross-validation of the PCA data yielded a low accuracy of 0.17 (± 0.086).

In order to determine which measures provided the most information in the LDA classification, we performed the LDA using combinations of measures, from individual measures through all available measures, and estimated the accuracy of the classification across all cells by dividing the data into training and testing sets. The accuracy as a function of the number of combined measures is shown in Fig 6. As expected, the accuracy improves as new measures are added, up until about 6 parameters, at which point the accuracy plateaus. However, the overall *worst* accuracy continues to improve as more measures are added. The black line indicates the mean of the best 5 combinations of measures. From this we conclude that some of the measures are possibly redundant and that some measures may be non-informative. With 7 or 8 combined measures (where the largest number of combinations was tested), AP height, R_{in}, RMP, τ_h and I_{rate} occurred together in each of the 5 most accurate runs. Similar, but not identical distributions were present for 8 combined measures. Note that the accuracy of each point includes a standard deviation estimate (not shown) as it is the result of multiple runs with different subsamples of training and test cells, so the best measures can vary with an arbitrary threshold, and there is no single "optimal" set. With the number of cells in the sample and the large number of parameters, the SD can be 15–20% of the mean value.

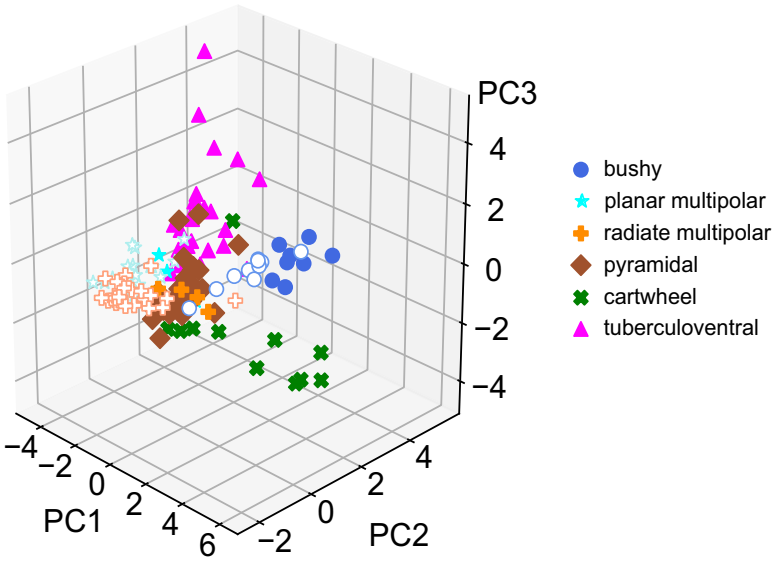

Fig 5. Principal components analysis (PCA) on the same data set as Fig 4. The PCA method is not supervised by cell type, and so the results depend only on factors that maximize the variance. The PCA successfully separated the cell classes, but did not have good accuracy with cross-validation. The view shown is the same format as Fig 4A.

https://doi.org/10.1371/journal.pone.0223137.g005

To further investigate those factors that drove the prediction accuracy, we performed the same analysis using the R package flipMultivariates. Table 1 summarizes the prediction accuracy by cell type, and provides mean measures for each of the parameters. Although all parameters provide a significant contribution (r^2) to the separation, the five that accounted for the largest proportions of the variance ($r^2 > 0.50$) were the AP height, AP half width, the adaptation measure, the coefficient of variation of interspike intervals, and the firing rate slope (I_{rate}). However, all of the measures showed a significant contribution.

Fig 7 plots the overall prediction accuracy against the observed classifiers. Although the overall accuracy was fairly high (87.1%), there were several confounds. The most common of these was radiate vs. planar multipolar, which occurred in about 25% of the cells in these groups. The next most common confound was misclassifying planar multipolar and tuberculoventral cells as pyramidal cells, followed by pyramidal cells being misclassified as tuberculoventral and planar multipolar cells. As these cells all fire regularly, and have similar measures on other properties, this is not surprising.

Discussion

We find that cells thoughout the cochlear nucleus can be objectively classified by firing patterns, action potential shapes, and responses to hyperpolarizing steps, as well as their morphology. While there is a long history of using specific electrophysiological features as identifying characteristics for different morphological cell classes in the CN, this work extends these comparisons across cell classes that fire regularly, and applies these measures to a population of cells taken from adult mice. In addition, these results suggest that cells can be classified according to their electrophysiological signatures, and the clearest classification requires consideration of a constellation of measurements.

With our data set, we found that the linear discriminant analysis can be used to classify cells based on the 12 measured electrophysiological features with ~80% success, although there was little improvement when using more than 7 parameters. This requires that the LDA

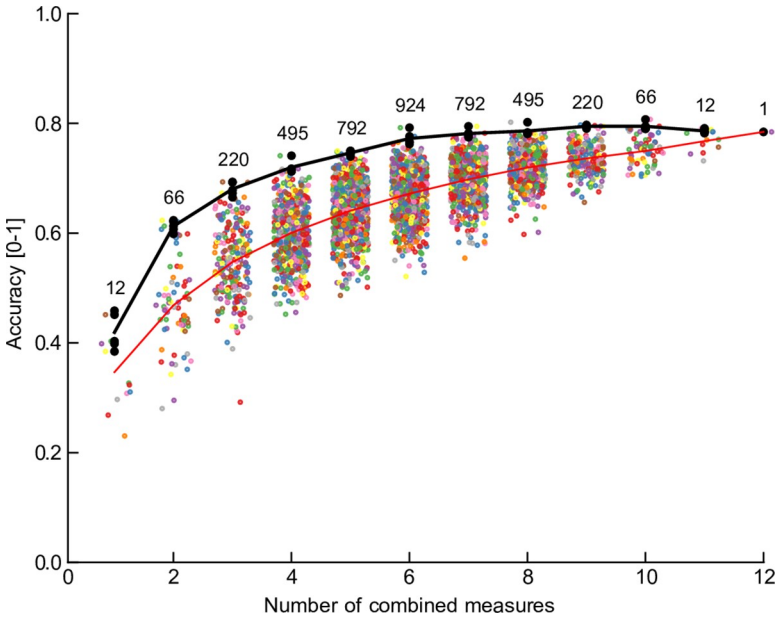

Fig 6. Accuracy of separation for different number of combined measures, using the LDA separation score for each set of measures. All 12 measures were considered in all possible combinations in groups from 1 to 12 (the number of combinations are shown above the data), and each combination is plotted as a point along the ordinate representing the number of combinations. The mean score is indicated by the red line. The average of the best 5 scores for each combination set are plotted as a black line. In general, including more measures improves the accuracy of the separation of groups.

https://doi.org/10.1371/journal.pone.0223137.g006

coefficients be estimated from a standardized (training) set of cells before application to an unidentified population. The selection and quality of the training data set is critical to the success of the technique. Cell morphology should be positively identified, and ambiguous cases

Table 1. Predictors and number of correct predictions.

Measure	Bushy	Planar multipolar	Radiate Multipolar	Pyramidal	Cartwheel	Tuberculo-ventral	R^2	p
RMP (mV)	-62.5	-62.7	-63.1	-68.5	-75.2	-67.9	0.41	<0.001
τ_m (ms)	1.29	4.90	2.83	8.04	5.25	12.71	0.41	<0.001
R_{in} (MΩ)	27.5	87.9	60.1	68.8	79.6	155.6	0.39	<0.001
τ_h (ms)	27.5	40.0	12.1	51.0	56.9	74.4	0.32	<0.001
B/A	0.50	0.63	0.39	0.59	0.95	0.71	0.28	<0.001
AP Height (mV)	-27.6	6.7	5.9	2.2	2.9	-6.9	0.63	<0.001
AP Width (ms)	1.32	0.26	0.28	0.40	0.83	0.35	0.73	<0.001
AP AHP (mV)	-57.7	-69.2	-68.3	-64.6	-53.8	-62.1	0.31	<0.001
AP Adaptation	0.96	0.05	0.21	0.10	0.22	0.13	0.62	<0.001
AP Rebound (N)	0.33	1.10	1.17	1.37	1.37	11.41	0.26	<0.001
CV	N/A	0.05	0.07	0.10	0.71	0.14	0.65	<0.001
I_{rate} (spikes/ nA)	5.8	1232	1158	412	768	1148	0.51	<0.001
Correct Predictions (%)	94.4	83.9	81.3	92.1	83.3	90.3		

Relations between the predictors and each cell class, indicating the number of correct predictions overall, and for each class. The top predicting variables (largest R^2 values) are indicated by shading. N = 162 cases used in estimation. Null hypotheses: two-sided; multiple comparisons correction: False Discovery Rate correction applied simultaneously to entire table. N/A: not applicable. See Methods and Materials for details of measurements.

https://doi.org/10.1371/journal.pone.0223137.t001

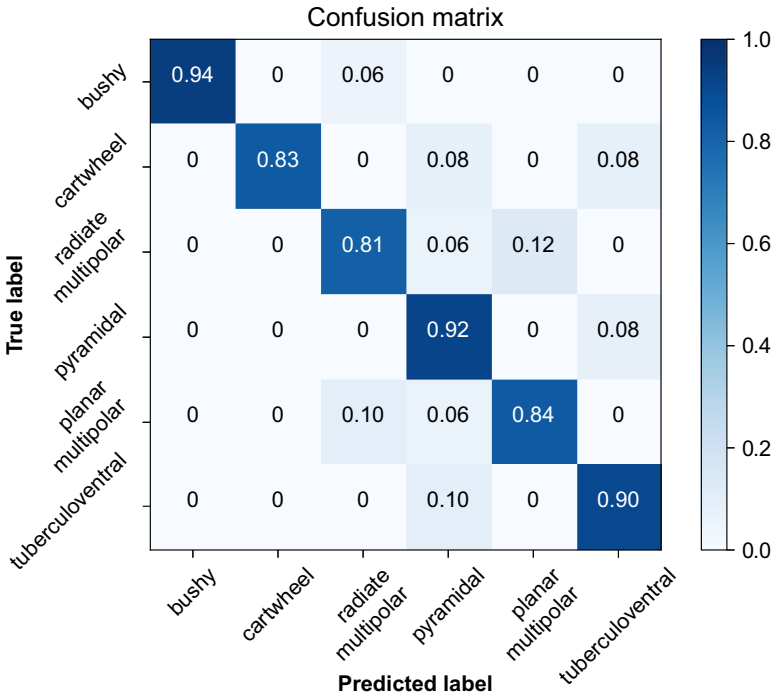

Fig 7. Prediction accuracy table (confusion matrix) by cell type. The most frequent mis-classifications occurred amongst cells with similar general firing patterns, such as planar and radiate multipolar cells, and pyramidal and tuberculoventral cells. This table was generated in R using data from all 12 measures. The numbers in each box indicate the proportion of correct classifications for each cell type.

https://doi.org/10.1371/journal.pone.0223137.g007

discarded in the training data, although it is essential to include a full range of cell properties in each class. The measurements should be complete and precise for each cell.

Our data set has three limitations in part because it was collected as part of a different experiments. The first is that due to different levels of hyperpolarizing current injection, the voltages reached with hyperpolarizing pulses were not consistent across cells, so that the estimates of the magnitude of the hyperpolarizing sag are influenced by the variability of the voltages reached. The second is that for depolarizing pulses, not all cells reached saturation of their firing rates. For this reason, we did not include maximal firing rates as a measure, but rather focused on the discharge rate and firing variability closer to spike threshold. A third limitation is that the current steps near spike threshold were, in some cells, too coarse to precisely define a threshold current. These limitations partly reflect the different input resistances of neurons; for example, hyperpolarizing pulses strong enough to damage tuberculoventral cells often fail to hyperpolarize pyramidal cells to -80 mV.

In addition, mis-classifaction could arise because of variability in the intrinsic excitability of cells even within a class, a low discriminability from the simple measures of excitability that were used, or it could represent mis-classification of a small fraction of the cells based on morphology. Although this latter error might arise to some extent in the VCN, particularly between the multipolar cell populations where incomplete filling of dendrites could confound assignments, it is less likely to be apparent in the DCN, where the 3 classes tested here have qualitatively distinct dendritic morphologies. The modest overlap between the pyramidal and tuberculoventral cells probably represents the limitations of the measurement features used, although it could also reflect a true confluence of intrinsic excitability. Alternatively, these results are also consistent with a wider physiological variability that leads to some overlap amongst morphological classes.

Classification errors principally occurred between cell classes with similar firing patterns, such as planar and radiate multipolar cells, and between pyramidal and tuberculoventral cells. These regular firing classes showed the largest dispersion along the 3rd component of the LDA. In contrast, bushy cells show significant dispersion in each of the first 3 dimensions of the LDA. This may indicate variability in the intrinsic excitability of these cell classes as noted before [12,44,45], or possibly the existence of distinct subclasses. This dispersion was also evident in the unsupervised PCA analysis. Substantially larger datasets of identified cells from individual strains would be needed to clarify the existence of such subclasses in the electrophysiology. An improvement in the classification would be expected to result from the inclusion of additional parameters such as maximal firing rates and the time courses of synaptic events.

Part of the dispersion in the VCN cell classes may also reflect strain or preparation differences, as the cells from CBA/CaJ mice were slightly offset from those from the NF107::Ai32 mice along the second LDA component. The strain difference is reminiscent of the differences in HCN channels seen in bushy, planar multipolar and octopus cells between ICR and a knockout on a hybrid 129S and C57Bl/6 background [3]. This raises a cautionary flag that the LDA should be trained on data acquired from cells recorded from animals of the same genetic background (and age and preparation techniques) if it is to be used to categorize cells from a novel data set.

In summary, we find that the major populations of CN neurons can be objectively classified against morphology with ~80% confidence based on electrophysiological signatures alone. This approach should be useful when comparing cells from different strains of mice or between different species, or between different experimental conditions such as animals with normal hearing and hearing loss. In addition, the distributions of features as determined here can be useful in setting and confirming parameters for models in which the cells of a given class are assigned a range of conductances in order to recapitulate the natural diversity seen experimentally.

Author Contributions

Conceptualization: Paul B. Manis.

Data curation: Paul B. Manis, Michael R. Kasten, Ruili Xie.

Formal analysis: Paul B. Manis, Ruili Xie.

Funding acquisition: Paul B. Manis, Ruili Xie.

Investigation: Michael R. Kasten, Ruili Xie.

Methodology: Paul B. Manis, Michael R. Kasten.

Project administration: Paul B. Manis.

Resources: Paul B. Manis.

Software: Paul B. Manis.

Visualization: Paul B. Manis.

Writing – original draft: Paul B. Manis.

Writing – review & editing: Paul B. Manis, Michael R. Kasten, Ruili Xie.

References

1. Rothman JS, Manis PB. Differential expression of three distinct potassium currents in the ventral cochlear nucleus. J Neurophysiol. 2003; 89: 3070–3082. https://doi.org/10.1152/jn.00125.2002 PMID: 12783951

2. Rothman JS, Manis PB. The roles potassium currents play in regulating the electrical activity of ventral cochlear nucleus neurons. J Neurophysiol. 2003; 89: 3097–3113. https://doi.org/10.1152/jn.00127.2002 PMID: 12783953
3. Cao X-J, Oertel D. The magnitudes of hyperpolarization-activated (I_h) and low-voltage-activated potassium (IKL) currents co-vary in neurons of the ventral cochlear nucleus. J Neurophysiol. 2011; 106: 630–640. https://doi.org/10.1152/jn.00015.2010 PMID: 21562186
4. Oertel D. Synaptic responses and electrical properties of cells in brain slices of the mouse anteroventral cochlear nucleus. J Neurosci. 1983; 3: 2043–2053. https://doi.org/10.1523/JNEUROSCI.03-10-02043.1983 PMID: 6619923
5. Wu SH, Oertel D. Intracellular injection with horseradish peroxidase of physiologically characterized stellate and bushy cells in slices of mouse anteroventral cochlear nucleus. J Neurosci. 1984; 4: 1577–1588. https://doi.org/10.1523/JNEUROSCI.04-06-01577.1984 PMID: 6726347
6. Oertel D, Wu SH, Garb MW, Dizack C. Morphology and physiology of cells in slice preparations of the posteroventral cochlear nucleus of mice. J Comp Neurol. 1990; 295: 136–154. https://doi.org/10.1002/cne.902950112 PMID: 2341631
7. Zhang S, Oertel D. Cartwheel and superficial stellate cells of the dorsal cochlear nucleus of mice: intracellular recordings in slices. J Neurophysiol. 1993; 69: 1384–1397. https://doi.org/10.1152/jn.1993.69.5.1384 PMID: 8389821
8. Zhang S, Oertel D. Giant cells of the dorsal cochlear nucleus of mice: intracellular recordings in slices. J Neurophysiol. 1993; 69: 1384–1397. https://doi.org/10.1152/jn.1993.69.5.1384 PMID: 8389821
9. Zhang S, Oertel D. Neuronal circuits associated with the output of the dorsal cochlear nucleus through fusiform cells. J Neurophysiol. 1994; 71: 914–930. https://doi.org/10.1152/jn.1994.71.3.914 PMID: 8201432
10. Manis PB, Spirou GA, Wright DD, Paydar S, Ryvgo DK. Physiology and morphology of complex spiking neurons in the guinea pig dorsal cochlear nucleus. J Comp Neurol. 1994; 348: 261–276. https://doi.org/10.1002/cne.903480208 PMID: 7814691
11. Xie R, Manis PB. Radiate and planar multipolar neurons of the mouse anteroventral cochlear nucleus: Intrinsic excitability and characterization of their auditory nerve input. Front Neural Circuits. 2017; 11: 77. https://doi.org/10.3389/fncir.2017.00077 PMID: 29093666
12. Kuo SP, Lu H-W, Trussell LO. Intrinsic and synaptic properties of vertical cells of the mouse dorsal cochlear nucleus. J Neurophysiol. 2012; 108: 1186–1198. https://doi.org/10.1152/jn.00778.2011 PMID: 22572947
13. Druckmann S, Hill S, Schürmann F, Markram H, Segev I. A Hierarchical Structure of Cortical Interneuron Electrical Diversity Revealed by Automated Statistical Analysis. Cereb Cortex. 2013; 23: 2994–3006. https://doi.org/10.1093/cercor/bhs290 PMID: 22989582
14. Tavakoli A, Schmaltz A, Schwarz D, Margrie TW, Schaefer AT, Kollo M. Quantitative Association of Anatomical and Functional Classes of Olfactory Bulb Neurons. J Neurosci. 2018; 38: 7204–7220. https://doi.org/10.1523/JNEUROSCI.0303-18.2018 PMID: 29976625
15. Tripathy SJ, Burton SD, Geramita M, Gerkin RC, Urban NN. Brain-wide analysis of electrophysiological diversity yields novel categorization of mammalian neuron types. J Neurophysiol. 2015; 113: 3474–3489. https://doi.org/10.1152/jn.00237.2015 PMID: 25810482
16. Typlt M, Englitz B, Sonntag M, Dehmel S, Kopp-Scheinpflug C, Ruebsamen R. Multidimensional characterization and differentiation of neurons in the anteroventral cochlear nucleus. PLoS One. 2012; 7: e29965. https://doi.org/10.1371/journal.pone.0029965 PMID: 22253838
17. Rao CR. The Utilization of Multiple Measurements in Problems of Biological Classification. J R Stat Soc Ser B. 1948; 10: 159–203. https://doi.org/10.2307/2983775
18. Gong S, Zheng C, Doughty ML, Losos K, Didkovsky N, Schambra UB, et al. A gene expression atlas of the central nervous system based on bacterial artificial chromosomes. Nature. 2003; 425: 917–925. https://doi.org/10.1038/nature02033 PMID: 14586460
19. Madisen L, Mao T, Koch H, Zhuo J, Berenyi A, Fujisawa S, et al. A toolbox of Cre-dependent optogenetic transgenic mice for light-induced activation and silencing. Nat Neurosci. 2012; 15: 793–802. https://doi.org/10.1038/nn.3078 PMID: 22446880
20. Xie R, Manis PB. Target-Specific IPSC Kinetics Promote Temporal Processing in Auditory Parallel Pathways. J Neurosci. 2013; 33: 1598–1614. https://doi.org/10.1523/JNEUROSCI.2541-12.2013 PMID: 23345233
21. Ting JT, Daigle TL, Chen Q, Feng G. Acute Brain Slice Methods for Adult and Aging Animals: Application of Targeted Patch Clamp Analysis and Optogenetics. Methods Mol Biol. 2014; 1183: 221–242. https://doi.org/10.1007/978-1-4939-1096-0_14 PMID: 25023312

22. Campagnola L, Kratz MB, Manis PB. ACQ4: an open-source software platform for data acquisition and analysis in neurophysiology research. Front Neuroinform. 2014; 8: 3. https://doi.org/10.3389/fninf.2014.00003 PMID: 24523692

23. Fujino K, Oertel D. Cholinergic modulation of stellate cells in the mammalian ventral cochlear nucleus. J Neurosci. 2001; 21: 7372–7383. https://doi.org/10.1523/JNEUROSCI.21-18-07372.2001 PMID: 11549747

24. Doucet JR, Ryugo DK. Projections from the ventral cochlear nucleus to the dorsal cochlear nucleus in rats. J Comp Neurol. 1997; 385: 245–264. PMID: 9268126

25. Campagnola L, Manis PB. A Map of Functional Synaptic Connectivity in the Mouse Anteroventral Cochlear Nucleus. J Neurosci. 2014; 34: 2214–2230. https://doi.org/10.1523/JNEUROSCI.4669-13.2014 PMID: 24501361

26. Lauer AM, Connelly CJ, Graham H, Ryugo DK. Morphological Characterization of Bushy Cells and Their Inputs in the Laboratory Mouse (Mus musculus) Anteroventral Cochlear Nucleus. PLoS One. 2013; 8: e73308. https://doi.org/10.1371/journal.pone.0073308 PMID: 23991186

27. Cant NB, Morest DK. Organization of the neuorns in the anterior division of the anteroventral cochlear nucleus of the cat. Light-microscopic observations. Neuroscience. 1979; 4: 1909–1923. https://doi.org/10.1016/0306-4522(79)90065-4 PMID: 530438

28. Webster DB, Trune DR. Cochlear nuclear complex of mice. Am J Anat. 1982; 163: 103–130. https://doi.org/10.1002/aja.1001630202 PMID: 7072613

29. Tolbert LP, Morest DK, Yurgelun-Todd DA. The neuronal architecture of the anteroventral cochlear nucleus of the cat in the region of the cochlear nerve root: horseradish peroxidase labelling of identified cell types. Neuroscience. 1982; 7: 3031–3052. https://doi.org/10.1016/0306-4522(82)90228-7 PMID: 6298659

30. Blackstad TW, Osen KK, Mugnaini E. Pyramidal neurones of the dorsal cochlear nucleus: A golgi and computer reconstruction study in cat. Neuroscience. 1984; 13: 827–854. https://doi.org/10.1016/0306-4522(84)90099-x PMID: 6527780

31. Lorente de No R. The Primary Acoustic Nuclei. NY: Raven Press; 1981.

32. Molitor SC, Manis PB. Dendritic Ca 2+ Transients Evoked by Action Potentials in Rat Dorsal Cochlear Nucleus Pyramidal and Cartwheel Neurons. J Neurophysiol. 2003; 89: 2225–2237. https://doi.org/10.1152/jn.00709.2002 PMID: 12612001

33. Mugnaini E, Berrebi A, Dahl A, Morgan J. The polypeptide PEP-19 is a marker for Purkinje neurons in cerebellar cortex and cartwheel neurons in the dorsal cochlear nucleus. Arch Ital Biol. 1987; 126: 41–67. Available: papers2://publication/uuid/CE9BAF51-50D1-4BC3-BA4B-D527E29C0730 PMID: 3449006

34. Wouterlood FG, Mugnaini E. Cartwheel neurons of the dorsal cochlear nucleus: A Golgi-electron microscopic study in rat. J Comp Neurol. 1984; 227: 136–157. https://doi.org/10.1002/cne.902270114 PMID: 6088594

35. Zhang S, Oertel D. Tuberculoventral cells of the dorsal cochlear nucleus of mice: intracellular recordings in slices. J Neurophysiol. 1993; 69: 1409–1421. https://doi.org/10.1152/jn.1993.69.5.1409 PMID: 8389823

36. Manis PB. Membrane properties and discharge characteristics of guinea pig dorsal cochlear nucleus neurons studied in vitro. J Neurosci. 1990; 10: 2338–2351. https://doi.org/10.1523/JNEUROSCI.10-07-02338.1990 PMID: 2376777

37. Hirsch JA, Oertel D. Intrinsic properties of neurones in the dorsal cochlear nucleus of mice, in vitro. J Physiol. 1988; 396: 535–548. https://doi.org/10.1113/jphysiol.1988.sp016976 PMID: 2457693

38. Kanold PO, Manis PB. Transient Potassium Currents Regulate the Discharge Patterns of Dorsal Cochlear Nucleus Pyramidal Cells. J Neurosci. 1999; 19: 2195–2208. https://doi.org/10.1523/JNEUROSCI.19-06-02195.1999 PMID: 10066273

39. Street SE, Manis PB. Action potential timing precision in dorsal cochlear nucleus pyramidal cells. J Neurophysiol. 2007; 97: 4162–4172. https://doi.org/10.1152/jn.00469.2006 PMID: 17442767

40. Leao RM, Li S, Doiron B, Tzounopoulos T. Diverse levels of an inwardly rectifying potassium conductance generate heterogeneous neuronal behavior in a population of dorsal cochlear nucleus pyramidal neurons. J Neurophysiol. 2012/03/02. 2012; 107: 3008–3019. https://doi.org/10.1152/jn.00660.2011 PMID: 22378165

41. Weedman DL, Pongstaporn T, Ryugo DK. Ultrastructural study of the granule cell domain of the cochlear nucleus in rats: mossy fiber endings and their targets. J Comp Neurol. 1996; 369: 345–360. https://doi.org/10.1002/(SICI)1096-9861(19960603)369:3<345::AID-CNE2>3.0.CO;2-5 PMID: 8743417

42. Apostolides PF, Trussell LO. Superficial stellate cells of the dorsal cochlear nucleus. Front Neural Circuits. 2014; 8: 1–9. https://doi.org/10.3389/fncir.2014.00001 PMID: 24478635

43. Mugnaini E, Sekerková G, Martina M. The unipolar brush cell: A remarkable neuron finally receiving deserved attention. Brain Res Rev. 2011; 66: 220–245. https://doi.org/10.1016/j.brainresrev.2010.10.001 PMID: 20937306

44. Francis HW, Manis PB. Effects of deafferentation on the electrophysiology of ventral cochlear nucleus neurons. Hear Res. 2000; 149: 91–105. https://doi.org/10.1016/s0378-5955(00)00165-9 PMID: 11033249

45. Cao X-J, Shatadal S, Oertel D. Voltage-sensitive conductances of bushy cells of the Mammalian ventral cochlear nucleus. J Neurophysiol. 2007; 97: 3961–3975. https://doi.org/10.1152/jn.00052.2007 PMID: 17428908